

Scaled-up synthesis of freestanding molybdenum disulfide membranes for nanopore sensing

Mohammad Amin Alibakhshi^{1*}, Xinqi Kang², David Clymer^{3,†}, Zhuoyu Zhang⁴, Anthony Vargas¹, Vincent Meunier^{3†}, Meni Wanunu^{1,2*}

Two-dimensional (2D) materials, owing to their extremely low thickness, are ideal materials for nanopores with optimal detection sensitivity and resolution. Among 2D materials, molybdenum disulfide (MoS₂) has gained significant traction as a more suitable nanopore material compared to graphene, which is much more hydrophobic. However, performing experiments using 2D nanopores remains challenging due to the lack of scalable fabrication methods of high-quality freestanding membranes. Here we report a site-directed, scaled-up synthesis of MoS₂ freestanding membranes on predrilled nanoapertures on 4-inch wafer substrates with 75% yields. A unique chemical vapor deposition (CVD) method that introduces sulfur and molybdenum dioxide vapors across both sides of the sub-100 nm nanoapertures results in the exclusive formation of freestanding membranes that seal the apertures. Nucleation and growth near the nanoaperture edges is followed by nanoaperture decoration with MoS₂ which proceeds until a critical flake radius of curvature is achieved, after which fully spanning freestanding membranes form. Intentionally blocking flow of reagents through the apertures inhibits MoS₂ nucleation around the nanoapertures, thereby promoting the formation of large-crystal monolayer MoS₂ membranes. The *in situ* grown membranes along with facile membrane wetting and nanopore formation using dielectric breakdown enabled the recording of dsDNA translocation events at 1MHz bandwidth, unprecedented for 2D nanopores. The methods presented here are important steps towards the development of many applications requiring single-layer membranes built at-scale in high-throughput 2D nanofluidics and nanopores studies.

¹ Department of Physics, Northeastern University, Boston, Massachusetts

² Department of Bioengineering, Northeastern University, Boston, Massachusetts

³ Department of Physics, Applied Physics, and Astronomy, Rensselaer Polytechnic Institute, Troy, New York

⁴ School of Physics, Nankai University, Tianjin 300071, P.R. China

[†]Current address: Department of Physics and Astronomy, University of Delaware, Newark, Delaware

[†]Current address: Department of Engineering Science and Mechanics, Penn State University, University College, PA

*E-mail: m.a.alibakhshi@gmail.com; wanunu@neu.edu

Application of protein nanopores as single-molecule third-generation sequencers^{1,2}

has shown great promise for fast and low-cost DNA/RNA sequencing, spurring the search for alternative pore materials that exhibit greater mechanical robustness,

This article has been accepted for publication and undergone full peer review but has not been through the copyediting, typesetting, pagination and proofreading process, which may lead to differences between this version and the [Version of Record](#). Please cite this article as [doi: 10.1002/adma.202207089](https://doi.org/10.1002/adma.202207089).

This article is protected by copyright. All rights reserved.

sharper pore geometries for improved resolution, and the ability to achieve higher throughput by massively-parallel fabrication methods. Solid-state nanopores with thicknesses that are comparable to the size of single nucleotides can revolutionize sequencing by enabling readout of shorter k-mers than current protein-based nanopores. However, solid-state nanopores, which have been dominated by silicon nitride (SiN), have proven to be less stable over time than protein nanopores because of limited chemical stability in electrolyte solution, particularly for membrane thickness around 1-5 nm. This limited stability of high-resolution SiN-based nanopores (and other ceramic-based pores) sets the stage for exploring various two-dimensional (2D) materials as possible replacements. Due to their crystalline atomically-thin nature, the family of 2D materials which includes graphene,³ hexagonal boron nitride,⁴ and transition metal dichalcogenides (TMDs) such as molybdenum disulfide (MoS₂) and tungsten disulfide (WS₂),⁵ exhibit excellent mechanical strength as well as exotic electronic and optical properties. Investigations of graphene nanopores for single-molecule sensing⁶⁻¹³ have demonstrated strong nonspecific hydrophobic interactions between graphene and DNA nucleotides⁸ and thus pore instabilities, as well as large values of low-frequency noise (1/f) during electrical measurements.¹⁴⁻¹⁶ In contrast, pores in TMD membranes such as MoS₂ are less hydrophobic, and also exhibit lower noise values than graphene pores, at the cost of a moderate increase in pore thickness. The thickness of monolayer MoS₂ nanopores accommodates 1-2 nucleotides at a time (assuming a stretched single strand in the pore), and thus, higher resolution than state-of-the-art protein pores could be achieved by direct trans-pore ion current measurements, or by coupling DNA translocation through the pore to transverse electronic current measurements,

where conductance modulations in the MoS₂ layer during DNA transport^{13,17-20} are used for basecalling.

While several studies employing MoS₂ nanopores have been reported to date, such as detecting DNA^{21,22} and its topological variations,²³ differentiating DNA monomers/homopolymers,²⁴ and detecting DNA methylation,²⁵ the overall number of devices made and datasets reported are relatively limited as compared to SiN-based or biological pores, owing to the major obstacle of producing freestanding MoS₂ membranes at high throughput. Typically, MoS₂ nanopore studies are carried out by manually transferring MoS₂ flakes onto apertures,²⁶ which complicates device manufacture and introduces polymer contaminations onto the membranes. We have previously shown that MoS₂ can directly grow in free-space without a substrate, to completely cover and seal 0.5-2 μm apertures.²² Nonetheless, understanding the growth mechanism remains elusive, and lack of sufficient control over microscopic quantities in terms of substrate quality and growth conditions has so far resulted in stochasticity in membrane formation and typically thick aperture coverage with many number of layers. As a result, given the small number of chips that can be accommodated in a 1" CVD tube that was used for MoS₂ growth, and given the larger apertures used (>1 μm), only a few devices per run were fabricated. Here, we expand this concept and demonstrate scaled-up and transfer-free synthesis of high-quality freestanding MoS₂ membranes on nanoscale apertures. We have identified 3 factors that were essential for reproducible formation of high-quality membranes: (i) aperture diameter, (ii) surface roughness, and (iii) gas flux through apertures. The effect of aperture diameter was verified through simulations, and the other two factors were experimentally found and addressed. Our first-principles quantum simulations elucidate the mechanism of freestanding membrane growth and provide

fundamental insight into the role of aperture size in successful formation of the freestanding membranes, which is linked to our observation of ring-like MoS₂ structures lining around the nanoaperture interior during growth. While with microapertures multiple nucleation and growth events can occur near the aperture, which result in typically thick and bulky membranes, growth across nano-apertures (<100 nm) is controlled by an interplay between the van der Waals energy between layers and the energy penalty of bending. Surface roughness was also found a critical factor in formation of the membranes, as protecting the apertures during microfabrication (by using single-side etcher, as well as PMMA coating, and later slight RIE etching) was essential for successfully growing freestanding membranes and reducing stochasticity in membrane growth and quality. Finally, in order to control the gas flux and timing, CVD tube had to be carefully setup in terms of amount of solid precursors, position of the wafers, temperature settings and ramps, etc. Transitioning to a 5-inch tube from a 1-inch tube results in an exponentially more complex process that is difficult to control, and therefore we relied on computational fluid dynamics (CFD) analysis of the CVD tube to gain a better understanding of the process, which helped with experimentally optimizing the process. We also devised a backing wafer bolted to a ceramic plate which was used to significantly reduce sulfur flux delivered to apertures and was key to a successful growth. Without such controls either excessive nucleation at the apertures takes place, or growth is terminated early without any membranes. Our method allows fabrication of many membrane devices (~200 devices from a 4" wafer) in a single growth run with the possibility of loading multiple wafers at the same time. Combined with voltage-assisted nanopore fabrication^{27,28}, this enables a route for MoS₂ nanopore studies. We obtain leakage-free, robustly anchored 2D membranes on nanoapertures which

contribute to high quality nanopore signals, also allowing investigations of 2D nanofluidic systems to advance our understanding of various anomalous transport behaviors at the nanoscale²⁹⁻³³ and the development of efficient filtration membranes. We further provide a quantitative comparison of this method with another method which does not rely on vapor flow through the apertures and guarantees uninterrupted growth of single MoS₂ crystals that span the nanoapertures, albeit at reduced yields. The fabrication yield of this non-selective growth method depends ultimately on surface coverage of the MoS₂ flakes, and thus achieving high-coverage growth on the entire 4" wafer area is key to high-yield fabrication. Finally, we demonstrate the first MHz-bandwidth recordings of DNA translocation through MoS₂ nanopores, in which we determine the fundamental impact of access resistance on the signal obtained during ultrafast DNA interaction with the pore (1-10 μ s timescales). The methods presented here allow high-yield MoS₂ device fabrication for high-throughput nanofluidics and nanopore studies.

Scaled-up synthesis of molybdenum disulfide 2D crystals. Many efforts have been devoted to the scaled-up growth of MoS₂ over large areas using CVD³⁴⁻³⁸ and metal-organic CVD (MOCVD) techniques.^{39,40} Generally, CVD growth results in higher crystal quality and a lower cost as compared to other techniques such as molecular beam epitaxy or atomic layer deposition. Nonetheless, use of solid precursors for CVD growth poses numerous challenges that include vaporization timing and flux supply, which limit the spatial uniformity and batch-to-batch repeatability. This problem becomes even more critical when growth over a large area is intended, since this requires a uniform thermal and reagent flux zone across a large diameter tube. Here, we used a two-furnace 5" diameter CVD tube with a 4.5" inner diameter (Supplementary Fig. 1), and the reagent boats and wafers were

arranged in the tube as shown in Fig. 1a. A sulfur powder is placed in a boat (shown on left of image), and a MoO_2 powder is spread on a source wafer and placed directly under the target wafer (i.e., the wafer that we intend to grow on) to provide a uniform MoO_2 supply during the growth phase (see Methods).

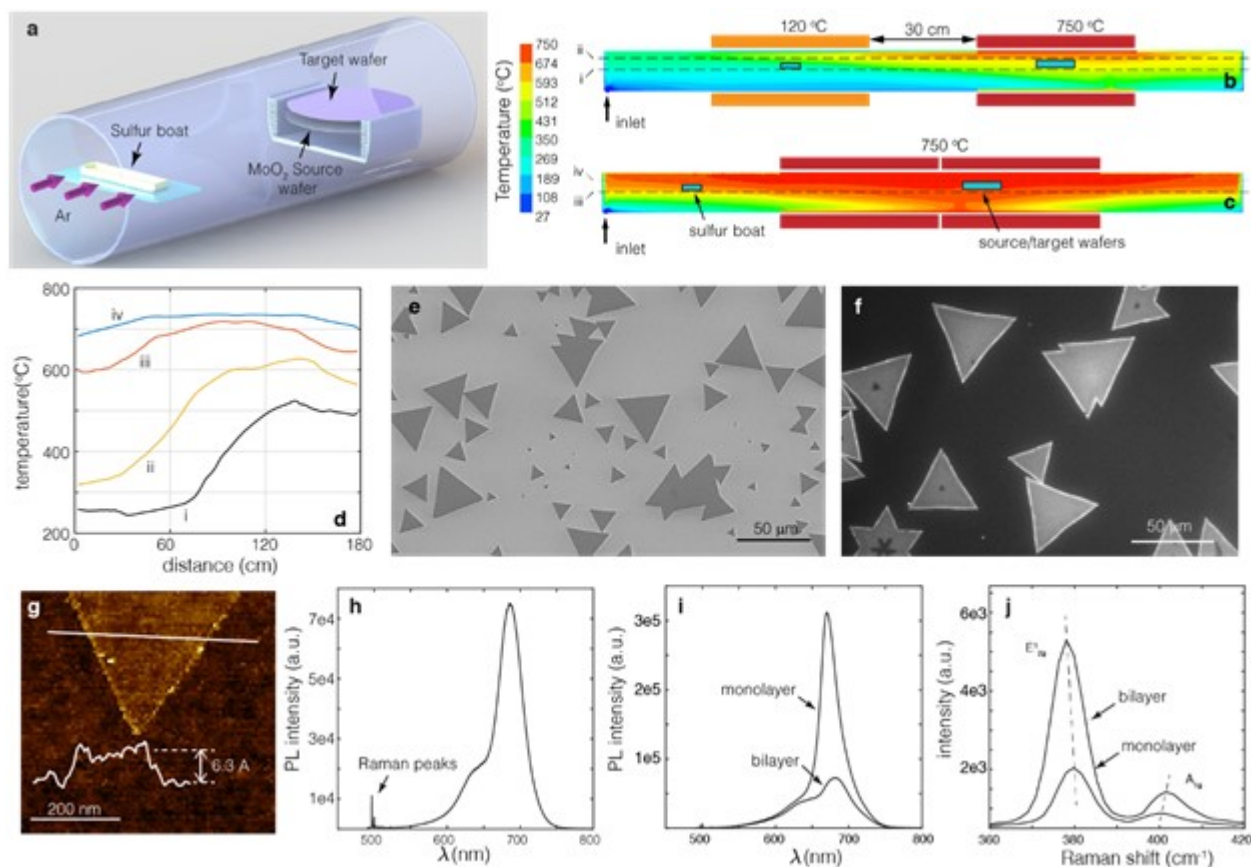


Fig. 1| Growth and characterization of MoS_2 crystals. **a**, Arrangement of the sulfur boat, MoO_2 (on source wafer) and the target wafer in a 5" quartz tube CVD furnace. **b,c**, Simulated temperature fields inside the tube for two different furnace configurations. The intended temperature for MoS_2 growth (750°C) cannot be achieved when only one furnace operates at this temperature. However, when both furnaces operate at 750°C and the gap between the two furnaces is eliminated, the proper thermal zone for MoS_2 growth is created. **d**, Temperature profiles along the tube at two locations (see dashed lines in **b** and **c**) for the two configurations (calculations are performed for steady-state while not accounting for radiation). **e**, Representative SEM image of MoS_2 grown on a Si/SiO_2 substrate. **f**, Photoluminescence intensity image of MoS_2 flakes enables identifying number of layers over large areas. **g**, Atomic force microscopy of a MoS_2 monolayer. Inset height profile along the white line indicates a single layer of MoS_2 . **h**, Photoluminescence emission spectrum of a monolayer MoS_2 crystal on a Si/SiO_2 substrate. **i**, Photoluminescence and **j**, Raman spectra of monolayer and bilayer flakes grown on a SiN substrate.

Failure to grow in this large tube with furnaces arranged as shown in Fig. 1b highlights the difficulty of achieving the required MoS_2 growth temperature. Our computational analysis (see Methods) indicates that setting the left furnace to 120°C

(to melt the sulfur) and the right furnace to 750°C (for MoO₂ sublimation and MoS₂ growth) with a gap in between results in strong density-gradient-driven secondary flows in the tube, which significantly contribute to heat loss from the tube (Supplementary Fig. 2). As a result, the intended temperature for growth at the target wafer position cannot be achieved (Fig. 1b). Setting the temperature of both furnaces to 750°C and placing them as shown in Fig. 1c supplies more heat to the growth region of the tube, reduces temperature loss near the target, and allows temperature to reach the intended value at the target wafer site (Figs. 1c and 1d), while allowing sulfur sublimation outside of the left tube. This configuration is also associated with a reduced axial flow velocity in the tube, and a smoother stream (Supplementary Fig. 2). We note that unlike the case of small tubes (1- or 2-inch diameter), where laminar axial flows develop, in the case of 5" diameter tubes large vortices can develop that fundamentally alter the temperature and flow profiles in the tube (Supplementary Fig. 2).

Upon addressing the heat loss from the tube, the temperature profile shown in Supplementary Fig. 3 was used in a typical growth (see Methods). An example of MoS₂ flake growth on a Si/SiO₂ substrate is shown in Fig. 1e. Since the AFM and photoluminescence measurements are time consuming and can be done on a limited number of spots on the wafer, we took advantage of 2D maps of PL intensities to examine very large areas over a short period of time. We equipped our microscope with a 470 nm collimated LED illumination (350 mW) and a 532 nm long pass emission filter to measure photoluminescence intensity from the entire microscope's field of view using a sensitive monochromatic CMOS camera (FLIR Grasshopper3). A PL image is shown in Fig. 1f wherein bright flakes are easily identifiable by their emission over a dark background, which is the characteristic of

monolayer MoS₂. Darker areas observed at the center of some of the flakes indicate thicker MoS₂ layers in self-seeded crystals.⁴¹ Examination of the flakes by atomic force microscopy (Dimension FastScan, Bruker) in several regions on the wafer indicates a 0.6-0.8 nm flake thickness (Fig. 1g), which confirms monolayer growth. We note that PL emission at the flake edges is brighter than the center of the flakes. A similar effect has been reported in WS₂ 2D crystals which was explained on the basis of chemisorption of oxygen atoms at the crystal edges.⁴² We also note that this effect is growth dependent, and in other cases the PL at the edge is darker than the center (Supplementary Fig. 4). Further quantification of the flakes with PL spectroscopy, shown in Fig. 1h (λ_{ex} = 488 nm = 2.54 eV), reveals a strong emission peak centered at 686 nm (1.81 eV). Such a monolayer growth can be guaranteed by carefully controlling the amount of MoO₂ as well as the gap between source and target wafers. A similar growth quality was observed on SiN substrates as evidenced by high PL intensities (Fig. 1i). Photoluminescence intensity significantly decreases for a bilayer flake. The Raman shift for a monolayer MoS₂ on the SiN substrate (λ_{ex} = 488 nm) was measured to be 20.1 cm^{-1} (Fig. 1j).

Selective growth on apertures. After achieving uniform growth across the entire 4” wafer area, we aimed at wafer-scale growth of freestanding MoS₂ membranes across nanoscale apertures. Understanding the growth of 2D materials on non-planar surfaces is essential for developing methods for direct formation of freestanding 2D membranes. When out-of-plane substrate features (such as grooves, or holes) are smaller than typical flake size, the crystal growth responds to their presence through different scenarios. We grew MoS₂ on 4” wafers that have

been processed to contain arrays of 5x5 mm chips that have freestanding SiN membranes with a 50-100 nm diameter circular nanoaperture present on each membrane (Fig. 2a, see Methods). The nanoapertures provide a unique opportunity for selective growth – by locally mixing sulfur and MoO₂ vapors from either side of the membranes, MoS₂ preferentially grows on or near the nanoapertures (Fig. 2b). Controlling the vapor flux at the aperture is a very critical factor in formation of the freestanding membranes. The optimal MoO₂ vapor concentration at the apertures was achieved by setting the gap between the source and target wafers to 5 mm (Fig. 2b). In order to control the sulfur flux, we backed the nanopore wafer with another wafer so that the two wafers are in close contact and the only gap between them is due to flatness of the wafers. Based on our prime-grade wafers' total thickness variation (TTV), we estimate the average gap between the two wafers to be $\delta \approx 10 \mu\text{m}$. The two wafers were pressed against each other using a ceramic plate and a set of ceramic nuts/bolts as shown in Fig. 2c. The sulfur flux can be further adjusted by choice of the sulfur boat's surface area, as well as its location along the tube which dictates its temperature (Supplementary Fig. 5).

Inspection of the membranes under an optical microscope after growth indicates growth of large MoS₂ flakes on all SiN membranes, which confirms the selective growth mechanism (Fig. 2d, Supplementary Fig. 6). However, large-flake growth does not guarantee the formation of freestanding MoS₂ membranes across the nanoapertures. Further inspection of the apertures with a transmission electron microscope (TEM) indicates an unusual growth within the aperture that results in formation of freestanding membranes (Fig. 2e, Supplementary Fig. 7). We observe the formation of multiple layers of MoS₂ that resemble a multi-shell MoS₂ tube that decorates the aperture interior. The observed feature is structurally very similar to

earlier reported seeded growth where growth starts from a fullerene-like multi-shell structure formed around the seeds.^{41,43,44} This side-wall MoS₂ growth is clearly identifiable under TEM (Fig. 2f), and is the signature of the selective growth mechanism where the two reagents only meet at the aperture. We note that in order to conform to the circular shape of the aperture, several fault lines appear around the aperture. In a rare case in which growth around the aperture was terminated only after formation of the first layer (Fig. 2g) a faceted edge was created which further verified the folding of flakes at the aperture edge (see supplementary Fig. 8 for a monolayer/bilayer faceted aperture edge). Formation of such MoS₂ tubes is an indication of geometry-constrained growth which can be further employed for developing other 2D nanofluidic systems. The structure of flakes grown on sidewalls is schematically shown in Fig. 2h, in which the MoS₂ layers within the aperture bend at the edge and extend on the SiN membrane surface. In fact, the TEM images of the aperture vicinity always show a number of layers decorated in various forms around the apertures (Fig. 2i, Supplementary Fig. 9a-l). From purely thermodynamical arguments, this folding can only occur if the van der Waals energy between layers exceeds the energy penalty of bending, otherwise flakes do not bend and grow across the apertures. Fig. 2j displays the aperture edge where the freestanding membrane and the side-wall layers meet, and shows how a completely sealed MoS₂ membranes is formed. Finally, the high-angle annular dark field (HAADF) imaging of a membrane containing a nanopore (Fig. 2k) enables precise identification of the pore shape and lattice structure. Here, the Mo atoms are evident in this image as bright white dots. The expected hexagonal lattice of the monolayer MoS₂ membrane was confirmed by the electron diffraction pattern (inset).

Smoothness of the nanoaperture edge and its very close vicinity area is critical for the formation of the freestanding membranes. During the microfabrication process, this area may be roughened and this results in excessive nucleation during the MoS₂ growth (Supplementary Fig. 9m). We find that protecting the membranes with polymethyl methacrylate (PMMA) before etching the underlying oxide layer, combined with brief reactive ion etching of the SiN membranes after SiO₂ was etched during wafer preparation significantly improves the likelihood of formation of MoS₂ membranes (see Methods). Conversely, treating the SiN membrane with buffered oxide etch or phosphoric acid prevents growth of flakes and consistently results in growth of a mesh-like structure at the surface (Supplementary Fig. 9n,o). The average fabrication yield of freestanding MoS₂ membranes in three consecutive full-wafer growths was found to be 75%. To obtain this number, we broke away pieces from three wafers produced in different runs and inspected 142 chips under TEM, 107 of which contained MoS₂ freestanding membranes completely spanning the nanoapertures, 28 chips were not fully covered, and 7 chips showed excessive growth at the aperture (Supplementary Fig. 9p). This wafer-scale fabrication yield is similar to the transfer-based method of fabrication of MoS₂ membranes on 3" wafers.⁴⁵ Yet, our method avoids transfer and transfer-associated contamination, and growth around the aperture results in more stable, lower noise membranes. In order to estimate the number of layers in the freestanding membranes we drilled nanopores in the MoS₂ membranes using TEM to be able to probe the pore edge structure (Supplementary Fig. 7a-l, see insets). We find that membranes are typically 1-3 layers thick, many of them containing monolayer regions of arbitrary sizes. Such membranes are ideal for nanopore sensing purposes, as while the pore can be created in a thinner region, the overall electric noise is reduced due to the presence

of thicker regions on the freestanding portions of the membranes. Our observation of the presence of 1-3 layer thick membranes is consistent with the notion that MoS₂ membrane formation is self-limiting, i.e., reagent flux through the nanoaperture is blocked once a sealed membrane forms.

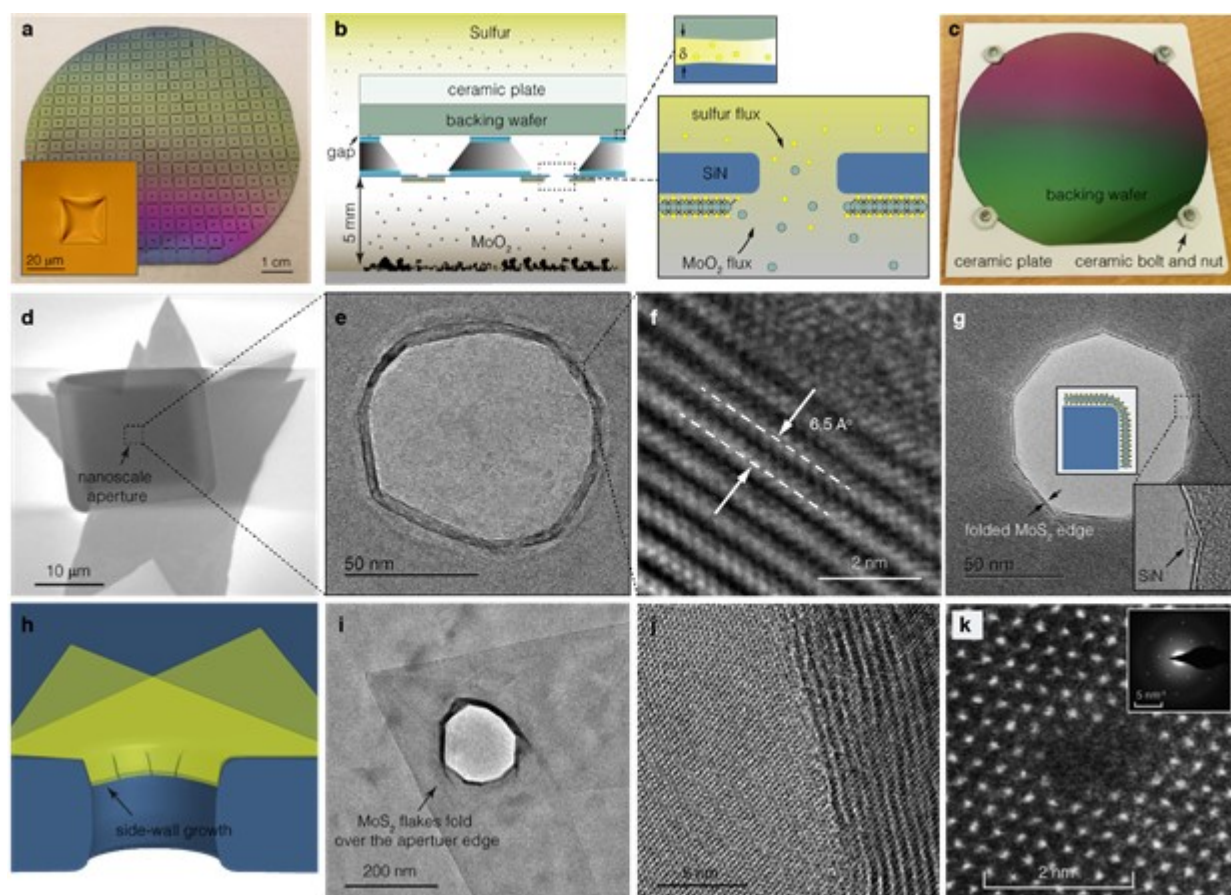


Fig. 2 | Selective MoS₂ growth on aperture. **a**, Bottom view (membrane side down) of a 4" Si wafer with 5 mm chips containing ~20 μm wide SiN freestanding membranes with a single nanoaperture. Inset: Optical image of the top side of the wafer, showing a 50-nm-thick freestanding SiN membrane (membrane buckle results from stress induced by the underlying SiO₂ layer on the membrane) **b**, Schematic of the arrangement of the source and target wafers (not to scale). The sulfur and MoO₂ vapors are brought each from one side of the aperture, which gives rise to selective growth across the aperture and its vicinity. **c**, A ceramic plate and a backing wafer are used to hold the target wafer and reduce diffusion of sulfur from the back of target wafer to the nanoapertures. The gap between the nanopore wafer and the backing wafer (δ) is identical to the flatness of the wafers which is estimated to be 10 μm . The target wafer is not shown here. **d**, Scanning electron micrograph of a freestanding SiN membrane after selective MoS₂ growth. Large flakes are formed on all SiN membranes that contain an aperture by locally mixing of sulfur and MoO₂ vapors. Apertures act like seeds where growth emanates from to its surrounding area. Formation of such flakes on the SiN membrane does not guarantee formation of a freestanding membrane that covers the aperture. **e**, Nanoaperture covered with a monolayer MoS₂ flake. Selective growth on the nanoaperture is characterized by vertically stacked MoS₂ layers at the edge, where multiple MoS₂ layers grow and fold to conform to the circular shape of the apertures, before a freestanding MoS₂ is formed. **f**, A close view of MoS₂ layers at the nanoaperture circumference. **g**, A faceted aperture edge formed by folding of a monolayer MoS₂ into the aperture. **h**, Schematic of the flakes folding at the aperture edge. **i**, An instance of MoS₂ growth in the immediate vicinity of apertures indicating the edge flakes fold back onto the substrate. **j**, A close view of the aperture edge demonstrate the vertically stacked MoS₂ layers, as well as the lattice structure of a MoS₂ freestanding membrane. **k**, HAADF imaging of monolayer MoS₂ after nanopore drilling using a STEM probe, showing the arrangement of the bright Mo atoms in the lattice (inset: electron diffraction pattern from a selected area on the freestanding MoS₂ membrane).

Numerical simulations

The electron microscopy images shown in Fig. 2 allow us to develop a mechanistic model for the single-layer membrane growth over the aperture. Experiments show that due to the specifics of the CVD growth setup, MoS₂ initially grows from both sides of the SiN wafer. This growth leads to the development of multiple MoS₂ layers that closely cover the contours of the SiN structure until an MoS₂ membrane appears to grow horizontally across the aperture. This step leads to drastic reduction in CVD activity since the presence of the membrane effectively prevents feedstock from reaching the top of the layer from below. We use elementary thermodynamic arguments to develop insight as to the existence of a crossover from the growth of bent MoS₂ layers espousing the SiN wafer into that of a quasi-flat, horizontal one covering the SiN aperture. As a starting point, consider that the high-resolution microscopy images shown in Fig. 2 can be described using the ball-and-stick model shown in Fig. 3a. We employed a first-principles approach based on density functional theory (DFT) to describe the energetics of why the lower MoS₂ layers bend around the SiN pore and the conditions for the appearance of horizontal growth. Two major terms contribute to the energetics: the energy penalty related to bending and the energy gain related to the stacking on the substrate. First, the uniaxial bending strain energy penalty is associated with the MoS₂ layer that bends to follow the outline of the SiN pore, going downward. The corresponding linear energy density is expressed per unit width of the membrane as:

$$E_b = \epsilon/R^2$$

Where R is the radius of curvature of the bent, and ϵ is the bending modulus of an MoS₂ membrane.⁴⁶ This relationship was verified using first-principles calculations on a series of armchair MoS₂ nanotubes as described in the Supplementary Information. DFT determines $\epsilon = 13.26 \pm 0.20$ eV Å per MoS₂ unit (Supplementary Fig. 21c). The number of MoS₂ units per unit cell is proportional to the radius of curvature as: $N_R = \alpha R$, where $\alpha = 2.44 \pm 0.02$ Å⁻¹ according to our DFT calculations applied to atomically relaxed structures (Supplementary Fig. 21b). The second energy term is a stabilization contribution due to van der Waals interactions between stacked layers:

$$E_{vdW} = \sigma A$$

Where $A = L/2 \times w$ is the surface area of absorption and $\sigma = 6.8$ meV/Å² as determined by DFT for MoS₂ (see details in Supplementary Information). Here L is the diameter of the SiN aperture and the factor $\frac{1}{2}$ is used since we only consider the energy for half a cell for both the bending and the van der Waals contributions (that is, we treat each side of the aperture separately). Taking into account the fact that in the bent configuration only $\frac{1}{4}$ of a tube is formed, the condition where a quasi-flat growth is thermodynamically more favorable than a bent geometry is met when $\frac{E_b w N_R}{4} > E_{vdW}$ and, in terms of experimental parameters, we find $L < L_{max}$ with $L_{max} = \frac{\epsilon \alpha}{2R\sigma}$. It is difficult to estimate the radius of curvature R at the bent of the MoS₂ membrane around the aperture, but examination of the microscopy images indicates the radius to be fairly small, possibly as small as the inter-layer distance between MoS₂ sheets. To obtain an estimate of the radius of curvature, we built a large MoS₂ torus from a long (20,20) nanotube (See Fig. 3b). Because of its large tube diameter (i.e., inner diameter), relaxation at $T = 0$ K shows that the torus initially folds inside

itself to form a double-layer nanotorus structure. From Fig. 3b, one can estimate the radius of bending curvature to be indeed quite small, and the absence of a bulge at the rim confirms that R can be as small as a few angstroms. We used a range of values of R to plot Fig. 3c, and we find that a horizontal growth will be favored and a membrane will cover the pore as soon as the radius of the SiN aperture is smaller than $L \sim 40 \text{ nm}$ for R in the vicinity of the interlayer distance. In spite of its simplicity, this model provides a rationale for the crossover between of the formation of bent layers to that of a flat membrane. The key idea is that a membrane will form when the cost of bending can no longer be compensated by the stabilization due to van der Waals stacking. The reason why a membrane ends up forming is that the development of bent MoS_2 layers progressively reduces the effective pore radius and the latter will decrease until it reaches the energetic threshold where bending is no longer energetically compensated. The model predicts a surprisingly good estimate for the order of magnitude observed experimentally. We expect that the model underestimates the value of L_{max} , as we now explain. Our computational analysis allows us to account for an additional observed feature. Experimentally, the actual structure around the SiN aperture often shows a collection of kinks in the direction normal to the pore wall. These kinks can be explained by the curvature along the aperture openings as well as to imperfections in the SiN itself, similar to what has been shown in carbon nanotubes, for instance.⁴⁷ When taking into account the large energy penalty of kink formation (compared to the more modest one associated with the bend described above), we conclude that the crossover from bent to flat membrane is expected to occur at larger pore size since the van der Waals interaction needs to be larger to compensate for the presence of the kinks. The system size precludes a full DFT modeling of the kink formation. MD performed

at 400K shows the emergence of those kinks, as shown in Fig. 3b, thus qualitatively supporting the growth mechanism described here. In addition, we can confirm the spontaneous emergence of kinks using classical molecular dynamics in a “pushed” MoS₂ membrane (Fig. 3d) as well as in an MoS₂ torus geometry (described in the supplementary information) that is reminiscent of the local MoS₂ morphology around the aperture. The appearance of kinks and facets around the aperture, which relieves curvature-induced stress on the MoS₂ film, is in agreement with our experimental observations.

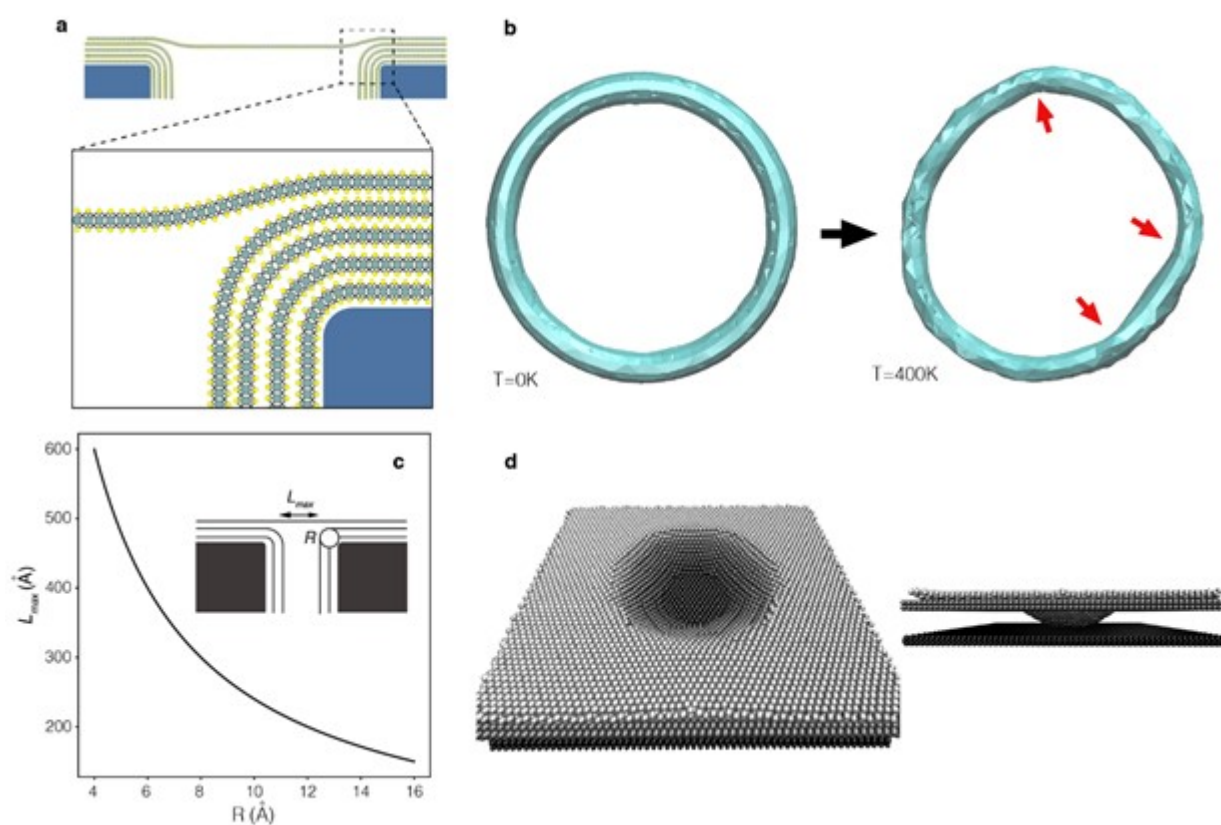


Fig. 3 | Growth model of MoS₂ across an aperture. **a.** Two predominant types of MoS₂ around a nanopore: initially MoS₂ growth follows the SiN pore with a combination of horizontal and vertical growth accompanied by a bent at the rim of the aperture. Eventually, an MoS₂ membrane growth exclusively horizontally across the aperture. **b.** A molecular dynamics simulation of a large MoS₂ torus confirms the value of inner radius around 7 Å. Further, molecular dynamics run at higher temperature indicates that the stress due to local curvature is spontaneously released by the presence of kinks (marked by red arrows), in agreement with experimental images shows in Fig. 2. **c.** A model of the growth energetics involves the stabilization energy due to vdW

stacking and the destabilization energy due to bending. This balance favors a mixed horizontal/vertical growth until the diameter of the aperture is below a limit L_{max} that depends on the effective radius of curvature R of the bent, as shown in the insert. Based on this, and for a radius of curvature of the order of the interlayer spacing, a horizontal membrane is predicted to form for aperture of the order of 40 nm in diameter. **d.** Two views of a 57 nm diameter pore decorated with MoS₂ after a molecular dynamics simulation, indicating how MoS₂ bends downward to closely follow the structure of the pore. This simulation also shows the onset of appearance of stress-releasing kinks along the rim, observed by facet formation.

Nonselective growth of membranes. Selective MoS₂ membrane growth on nanoapertures is an effective method of scaled-up synthesis, which requires delicate preparation of the aperture, as well as control of vapor flux through the apertures. On the other hand, the fact that a growing MoS₂ flake follows the surface morphology, inspired an alternative sacrificial layer-based fabrication scheme (Fig. 4a). The SEM and AFM images of MoS₂ grown on a model substrate entirely patterned with microcavities (2.5 μm diameter, 40 nm deep, and 25 μm pitch) confirm that when MoS₂ flakes meet a groove growth is not interrupted, and instead follows the surface profile and conformally coats the substrate (Fig. 4b,c). Therefore, by growing MoS₂ on a microcavity nanowell backed by a sacrificial layer and establishing an orthogonal chemistry for selectively etching the sacrificial layer without etching the MoS₂, a freestanding membrane was formed. In this method, formation of the membranes relies on coincidental growth of flakes on cavities, and thus we refer to it as the nonselective growth. In this case, the likelihood of freestanding membrane formation is proportional to the overall coverage of the wafer with MoS₂ flakes, and it becomes essential to achieve high coverage growths.

Supplying uniform flux of both reagents onto the target wafer is key to obtaining a high coverage and uniform growth (Supplementary Fig. 10). By spraying an MoO₂/IPA suspension mix on a perforated wafer (Figs. 4d), not only was MoO₂ dispensed evenly on the entire source wafer, but also the holes on this source wafer

allowed sulfur transport through the wafer (Fig. 4e, see inset) and uniform showering on the target wafer (see Methods for details). Figs. 4f-h show the coverage map and the crystal size map of a typical growth with this method, along with microscope images of the flakes on different spots on the wafer. Here, 50% of the wafer surface area is covered by MoS₂ flakes without using any seeding, with some regions reaching 100% film coverage (Supplementary Fig. 11). The triangular shapes of all the flakes indicate very uniform supply of MoO₂ and sulfur vapors over the entire area with our method, or else hexagonal- and star-shaped flakes would be observed.⁴⁸ We have obtained similar growth for Si/SiO₂ substrates, Si/SiN substrates, and Si/SiO₂/SiN substrates which are the wafers used for SiN nanoaperture fabrication. Flake size and coverage can be conveniently regulated by controlling the MoO₂ mass and the gap between the source and target wafers.

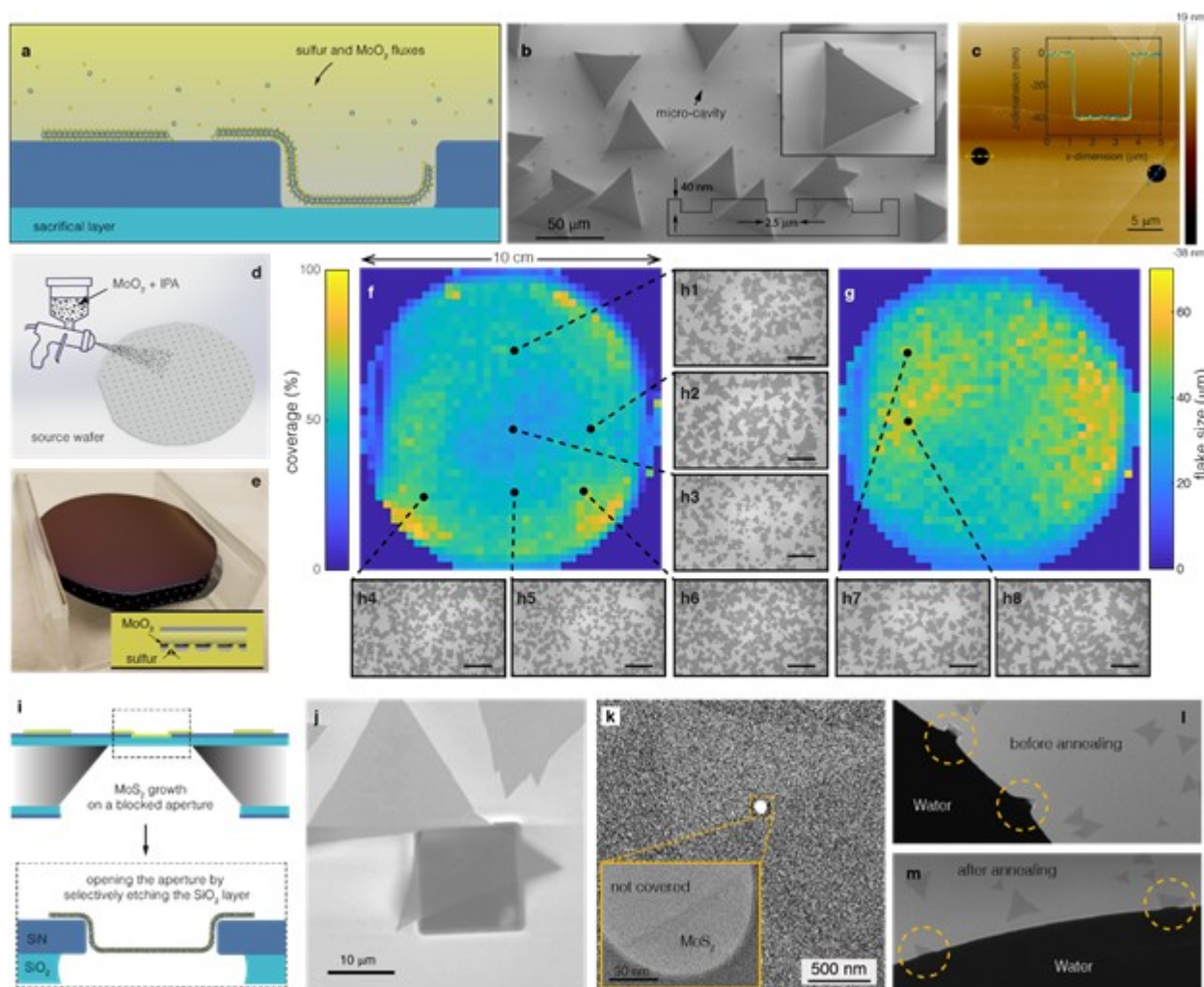


Fig. 4 | High coverage MoS₂ growth, and nonselective growth of MoS₂ across apertures. **a**, Schematic of MoS₂ growth on a grooved substrate. **b**, SEM image of MoS₂ flakes grown on a 4-inch substrate entirely patterned with micro-cavities. **c**, AFM image of a flake grown on the grooved substrate indicating flakes conformally coat the substrate. **d**, Uniform coating of MoO₂ powder on the perforated source wafer was obtained by spraying a suspension of MoO₂ in IPA. **e**, Quartz boat devised for horizontal positioning of the wafers in the tube and controlling the gap between the two wafers. The source wafer (bottom) contains through-holes which improve growth uniformity by allowing sulfur to diffuse through the wafer (see inset). **f**, Map of MoS₂ coverage on a representative growth indicates an average 50% coverage. A motorized stage synchronized with a camera captured images with 2.5 mm pitch. **g**, Map of flake size on the same wafer. **h1-h8**, Snapshots of MoS₂ growth at different indicated spots on the wafer (Scale bars = 200 μm). **i**, Schematics of the nonselective growth method. Likelihood of covering the apertures in this method is proportional to the overall coverage of the nanopore wafer with MoS₂ flakes. The SiO₂ layer is removed after MoS₂ is grown on the wafer. **j**, Scanning electron microscope image of a flake coincidentally grown on a SiN membrane, covering the aperture (image recorded after the silicon oxide layer was removed). **k**, An MoS₂ freestanding membrane fabricated with this method partially covering the aperture. Blocking the gas flux through the aperture eliminates side-wall growth, and unlike the selective growth method, flake growth occurs irrespective of the aperture location. **l, m**, Images of water receding from a flake-containing wafer before (**l**) and after (**m**) annealing, illustrating the transition from hydrophilic to semi-hydrophobic MoS₂ flakes grown on a SiN substrate. Annealing stabilizes the adhesion of MoS₂ flakes to the substrate upon immersion in buffers.

In fabrication of the nanopore wafers, the SiN layer is always deposited on a SiO₂ layer, which serves to reduce the capacitive noise of our devices (see Methods).

This SiO₂ layer can also serve as the sacrificial layer, owing to the orthogonal chemistry that it forms with MoS₂ and the buffered oxide etch (BOE), which enables selective etching of the SiO₂ layer⁴⁹ and release of MoS₂ freestanding membranes (Fig. 4i). Therefore, in preparation of the wafers, after etching the apertures through the SiN layer, this SiO₂ layer is not removed until after the MoS₂ grown on the wafer (Figs. 4i,j). This method results in very uniform coating of the apertures, without excessive nucleation and growth around the aperture (Figs. 4k, Supplementary Fig. 12). We further note that the apertures blocked by silicon oxide are invisible to the growth, as neither side-wall growth on the aperture (the MoS₂ tubes) occurs in this method, nor the direction of growth changes when a flake meets the aperture edge (Fig. 4k).

Upon exposure to aqueous medium, buffers, or organic solvents flakes were observed to wrinkle, roll up, or in some cases float (Supplementary Fig. 13). Annealing wafers in argon environment (containing 5% hydrogen) at 400°C at 50 Torr for 5 hours was observed to resolve this problem. This is an essential step in our process and stabilizes the MoS₂ flakes in solution. This step reduced the relative hydrophilicity of the flakes as evidenced by water contact angle experiments. Fig. 4l shows a water droplet placed on a substrate before annealing. We observe water at the droplet edge spreads on the flakes indicating smaller contact angles on the flakes compared with the substrate. After droplet edge recedes due to evaporation, the flakes are observed to have rolled up (Supplementary Fig. 13). After annealing, however, the water contact angle on the substrate and flakes became very close (Fig. 4m) and the flakes remained adherent to the substrate. We further note that UV ozone treatment helps to maintain flake adhesion to the substrate during immersion in solution, which suggests that matching surface energies between the flakes and

the substrates promotes their stability upon immersion, while mismatched surface energies promote flake roll-up and wrinkling upon immersion. Despite the simplicity of this method and the smooth aperture coverage achieved, we find some variability in terms of etch resistance of the MoS₂ to BOE, which ultimately reduces the yield of this method (Supplementary Fig. 14). Addressing this seemingly growth dependent etch resistance is beyond the scope of this paper. Finally, after removing the SiO₂ layer and deionized water rinsing, if the apertures are too large (200 nm) the membrane may be pulled through the apertures (Supplementary Fig. 15), and therefore smaller aperture sizes are required to achieve stable freestanding MoS₂ using this method.

Nanopore sensing. Next, we characterized ion current leakage and electrical noise through our freestanding MoS₂ membranes by performing trans-membrane conductance measurements (see Methods). After mounting the devices in a fluidic flow cell, a freestanding MoS₂ membrane separates two electrolyte-filled reservoirs, such that in the presence of a nanopore, application of an electric field across the membranes creates a steady ionic current (Fig. 5a, inset). In the absence of a nanopore, any DC current recorded can be attributed to the membrane leakage. Nonetheless, measuring the current leakage is difficult, as we first need to ensure the MoS₂ membrane is fully wet on both sides of the membrane. This is particularly challenging in 2D nanopores due to their hydrophobicity. Here we find that for MoS₂ membranes a rapid pretreatment of the membrane with acetonitrile (CH₃CN) can significantly facilitate subsequent hydration. Membrane wetting can be confirmed in the absence of a nanopore by observing a longer RC time constant in the transient

capacitive current when a voltage step is applied, than for a membrane occluded with an air bubble. We find that in the absence of a nanopore no appreciable conductance can be measured for a wet membrane (<10 pS, which has contributions from the capacitive response too), indicating a complete membrane seal in our apertures. Another indication of wetting is the fact that a nanopore could be punctured by a brief application of a <1 V voltage bias, presumably through a dielectric breakdown (also referred to electrochemical reaction) mechanism. We mainly used voltage-induced poration to form nanopores since voltage induces the highest electric field on the thinnest regions of our membranes, thereby favoring the formation of single-layer-thick pores.

The $i - v$ curves of seven different nanopores in the diameter range of 2-4 nm are shown in Fig. 5a. Three of these pores were drilled using TEM and others were formed by dielectric breakdown. We use the nanopore conductance to estimate the pore diameter through $G = K \left(\frac{1}{D} + \frac{4l}{\pi D^2} \right)^{-1}$, with K being the electrolyte conductivity, D the pore diameter, and l the pore thickness. For these ultrathin MoS₂ membranes access resistance is the dominating term and thus the conductance can be estimated by $G = KD$. Ionic current traces recorded at 0 mV and 200 mV and lowpass-filtered at various cutoff frequencies, along with corresponding rms noise values are shown in Fig. 5b. Below 100 kHz, the rms noise significantly increases with increasing the applied voltage, while above 100 kHz rms noise values are similar. This can be further observed in the noise spectra at different voltages, which indicate larger contributions to the overall noise from the low-frequency regime, particularly as voltage increases (Fig. 5c). This $1/f$ noise is a characteristic of 2D nanopores which has been previously reported for graphene and MoS₂ nanopores.

Recent studies suggest that the $1/f$ noise originates from the surface conduction of the nanopore,¹⁵ and adsorption-desorption of ions at the pore surface which is coupled with the long-lasting excursions of the ions in the reservoirs.¹⁶ We note some variations in the contribution of the low frequency components to the total rms noise from device to device (see data from another pore device in Supplementary Fig. 16), possibly due to the area of the monolayer region.

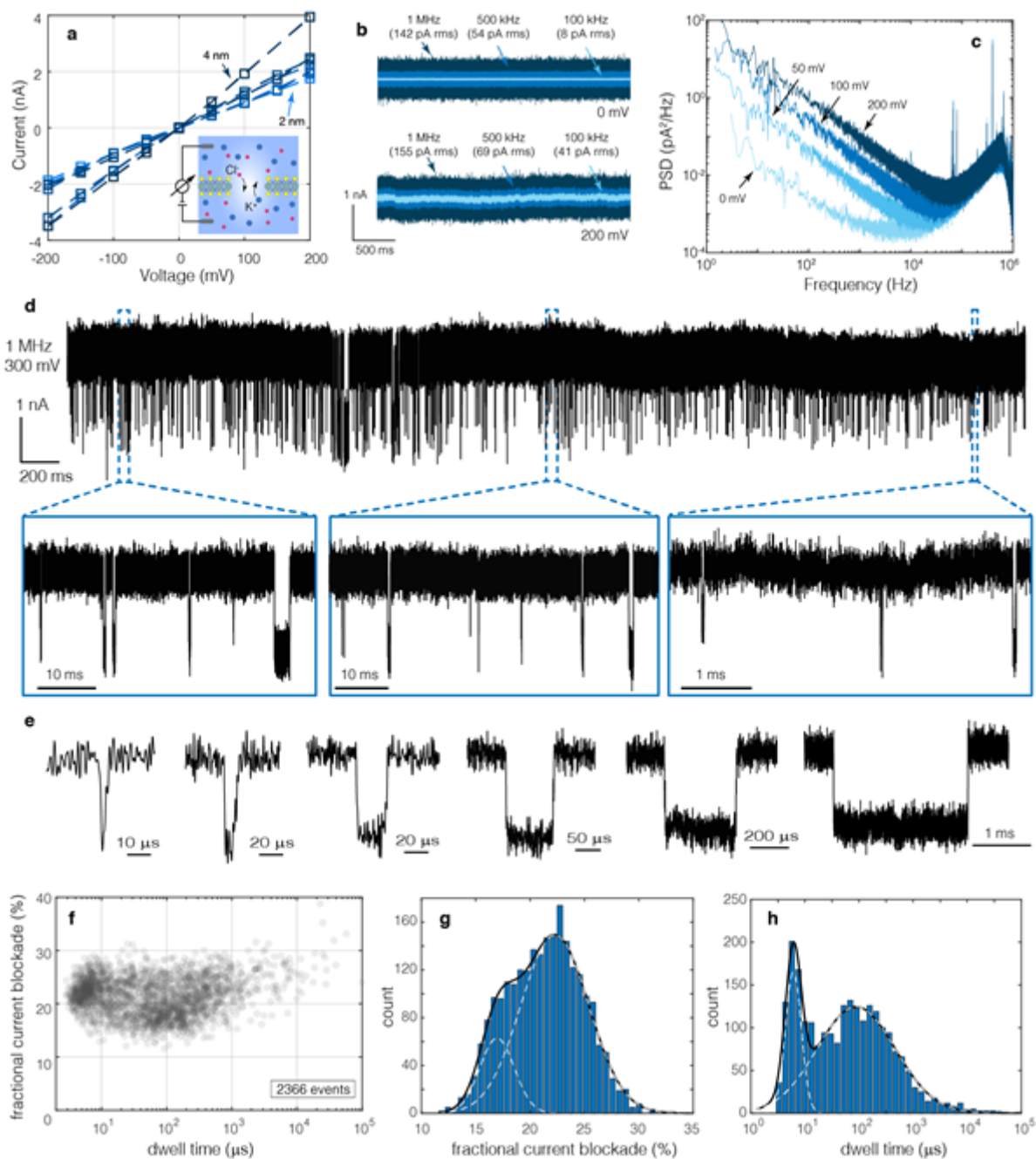


Fig. 5| Conductance, noise spectra, and DNA translocations through MoS₂ nanopores. **a**, Current vs. voltage measurements for different nanopores with diameters in the range of 2 - 4 nm. Nanopores are either drilled by a transmission electron microscope or by dielectric breakdown. Inset: Schematic illustration of a nanopore in a single-layer MoS₂ membrane that separates two electrolyte-filled reservoirs, such that ionic current can only be established through the nanopore. **b**, Current traces recorded at 0 mV and 200 mV, and lowpass filtered at different frequencies. **c**, Noise spectra of the ionic current recorded at different applied voltages. **d**, A current trace of a 4 nm diameter pore at 300 mV in the presence of 500 bp dsDNA, recorded at 1 MHz bandwidth. The nanopore was formed by voltage-induced breakdown. **e**, Representative translocation events occurring at different timescales. **f**, Scatter plot of fractional current blockade vs dwell time indicating two different populations corresponding to translocation events (slower) and DNA collision with the nanopore (fast). **g**, Distributions of fractional current blockades and **h**, dwell times for the data presented in panel **f**, which shows the characteristic timescales and signal amplitudes of collisions and translocations.

Fig. 5d shows a current trace of translocation of 500bp dsDNA through MoS₂ nanopores at 300 mV, with selected magnified views shown below the trace. The pore diameter which was formed with dielectric breakdown was estimated to be 4 nm. The 1MHz amplifier bandwidth (Chimera Instruments LLC, see Methods) enabled recording very fast translocations down to $\sim 2 \mu\text{s}$. Several representative translocation events with dwell times in the μs to ms range are shown in Fig. 5e. The scatter plot of fractional current blockades versus dwell times including 2,366 events is shown in Fig. 5f. The current trace used in the scatter plot was lowpass filtered at 500 kHz to allow better fitting of the events to square pulses. Two distinct populations are evident in the scatterplot. We attribute the fast population to DNA collision with the pore and the slow population to translocation events. We note that likelihood of collision with pore as opposed to translocation can be influenced by the pore shape, which is not known. The fractional current blockade of the translocating events is 17% (Fig. 5g) which agrees well with the theoretical estimation (Supplementary Fig. 17). In order to estimate the blockade, we assumed the access resistance of a nanopore ($R_{acc} = 1/KD$) during translocation is modified as $R_{acc} = 1/KD_{eff}$ with $D_{eff} = \sqrt{D^2 - d_{dsDNA}^2}$ ($d_{dsDNA} = 2.2 \text{ nm}$ is the cross-sectional diameter of dsDNA). The collision events are blocking slightly higher currents (22%). The mean dwell times for the two populations are $6_{-2.3}^{+3.8} \mu\text{s}$ and $88_{-80}^{+837} \mu\text{s}$ (st. dev).

In summary, we demonstrated MoS₂ growth over waferscale areas as large as 4" with high coverage without any need for seeding, and presented two schemes for scaled-up fabrication of MoS₂ freestanding membranes. Our study encompasses over 450 CVD runs, commencing with optimization of uniform growth on different wafer substrates without nanoapertures (Si/SiO₂, Si/SiN, and Si/SiO₂/SiN), and then

proceeding with selective growth optimization on 34 wafers containing SiN nanoapertures and 10 wafers with SiN micro-apertures (Supplementary Fig. 14.a). Over 1,050 chips were individually inspected using TEM, the most reliable method to confirm freestanding MoS₂ membrane formation. We found that selective growth proceeds by nucleation near or at the nanoapertures, and results in the formation of multiple flakes growing around the aperture, followed by freestanding membranes that span the aperture once the radius of curvature is too large to bend around the nanoaperture curvature. Focusing the vapor-phase reagents to the aperture is critical here to the selective growth, which enables formation of freestanding membranes with 75% yields across a 4" wafer. We have outlined here the roles of smoothness of the nanoaperture vicinity, controlled reagent flux, and critical aperture size on the successful formation of freestanding membranes. Further, we introduced an alternative method in which elimination of the trans-pore vapor flux suppresses excessive growth around the aperture, resulting in large MoS₂ flakes. Our MoS₂ membranes exhibit excellent seals, preventing ion flow through nanopore-free membranes and very low noise as compared with other pores in transferred 2D membranes. We have demonstrated the first high-bandwidth (1 MHz) measurements of DNA transport through a MoS₂ nanopore, highlighting the contribution of access resistance on the overall signal in sub-nm nanopore thicknesses. Our scaled-up method for synthesis of MoS₂ membranes accelerates various single-molecule measurements with 2D nanopores, and advances 2D nanofluidics research such as development of 2D filtration membranes.

References

- 1 Clarke, J. *et al.* Continuous base identification for single-molecule nanopore DNA sequencing. *Nature nanotechnology* **4**, 265-270 (2009).

- 2 Derrington, I. M. *et al.* Nanopore DNA sequencing with MspA. *Proceedings of the National*
3 *Academy of Sciences* **107**, 16060-16065 (2010).
- 4 Heerema, S. J. & Dekker, C. Graphene nanodevices for DNA sequencing. *Nature*
5 *nanotechnology* **11**, 127 (2016).
- 6 Liu, K. *et al.* Geometrical Effect in 2D Nanopores. *Nano Lett* **17**, 4223-4230,
7 doi:10.1021/acs.nanolett.7b01091 (2017).
- 8 Danda, G. *et al.* Monolayer WS₂ Nanopores for DNA Translocation with Light-Adjustable
9 Sizes. *ACS Nano* **11**, 1937-1945, doi:10.1021/acsnano.6b08028 (2017).
- 10 Crick, C. R., Sze, J. Y., Rosillo-Lopez, M., Salzmann, C. G. & Edel, J. B. Selectively sized
11 graphene-based nanopores for in situ single molecule sensing. *ACS applied materials &*
12 *interfaces* **7**, 18188-18194 (2015).
- 13 Waduge, P., Larkin, J., Upmanyu, M., Kar, S. & Wanunu, M. Programmed synthesis of
14 freestanding graphene nanomembrane arrays. *Small* **11**, 597-603 (2015).
- 15 Schneider, G. F. *et al.* Tailoring the hydrophobicity of graphene for its use as nanopores for
16 DNA translocation. *Nature communications* **4**, 2619 (2013).
- 17 Merchant, C. A. *et al.* DNA translocation through graphene nanopores. *Nano letters* **10**,
18 2915-2921 (2010).
- 19 Schneider, G. F. *et al.* DNA translocation through graphene nanopores. *Nano letters* **10**,
20 3163-3167 (2010).
- 21 S. Garaj, W. H., A. Reina, J. Kong, D. Branton & J. A. Golovchenko. Graphene as a
22 subnanometre trans-electrode membrane. *Nature* **467**, 190–193 (2010).
- 23 Garaj, S., Liu, S., Golovchenko, J. A. & Branton, D. Molecule-hugging graphene nanopores.
24 *Proceedings of the National Academy of Sciences* **110**, 12192-12196 (2013).
- 25 Traversi, F. *et al.* Detecting the translocation of DNA through a nanopore using graphene
26 nanoribbons. *Nature nanotechnology* **8**, 939 (2013).
- Heerema, S. *et al.* 1/f noise in graphene nanopores. *Nanotechnology* **26**, 074001 (2015).
- Fragasso, A., Pud, S. & Dekker, C. 1/f noise in solid-state nanopores is governed by access
and surface regions. *Nanotechnology* **30**, 395202 (2019).
- Gravelle, S., Netz, R. R. & Bocquet, L. Adsorption kinetics in open nanopores as a source of
low frequency noise. *Nano letters* (2019).
- Xie, P., Xiong, Q., Fang, Y., Qing, Q. & Lieber, C. M. Local electrical potential detection of DNA
by nanowire–nanopore sensors. *Nature nanotechnology* **7**, 119-125 (2012).
- Healy, K. *et al.* Fabrication and characterization of nanopores with insulated transverse
nanoelectrodes for DNA sensing in salt solution. *Electrophoresis* **33**, 3488-3496 (2012).
- Graf, M., Lihter, M., Altus, D., Marion, S. & Radenovic, A. Transverse detection of DNA using
a MoS₂ nanopore. *Nano Letters* **19**, 9075-9083 (2019).
- Heerema, S. J. *et al.* Probing DNA translocations with inplane current signals in a graphene
nanoribbon with a nanopore. *ACS nano* **12**, 2623-2633 (2018).
- Liu, K., Feng, J., Kis, A. & Radenovic, A. Atomically thin molybdenum disulfide nanopores with
high sensitivity for DNA translocation. *ACS nano* **8**, 2504-2511 (2014).
- Waduge, P. *et al.* Direct and Scalable Deposition of Atomically Thin Low-Noise MoS₂
Membranes on Apertures. *ACS Nano* **9**, 7352-7359, doi:10.1021/acsnano.5b02369 (2015).
- Liu, K. *et al.* Detecting topological variations of DNA at single-molecule level. *Nature*
Communications **10**, 3 (2019).
- Feng, J. *et al.* Identification of single nucleotides in MoS₂ nanopores. *Nature*
nanotechnology **10**, 1070 (2015).
- Shim, J. *et al.* Detection of methylation on dsDNA using nanopores in a MoS₂ membrane.
Nanoscale **9**, 14836-14845 (2017).
- Graf, M. *et al.* Fabrication and practical applications of molybdenum disulfide nanopores.
Nature protocols **14**, 1130-1168 (2019).

- 27 Kuan, A. T., Lu, B., Xie, P., Szalay, T. & Golovchenko, J. A. Electrical pulse fabrication of
graphene nanopores in electrolyte solution. *Applied physics letters* **106**, 203109 (2015).
- 28 Feng, J. *et al.* Electrochemical reaction in single layer MoS₂: nanopores opened atom by
atom. *Nano letters* **15**, 3431-3438 (2015).
- 29 Zhong, J. *et al.* Exploring Anomalous Fluid Behavior at the Nanoscale: Direct Visualization
and Quantification via Nanofluidic Devices. *Accounts of Chemical Research* **53**, 347-357
(2020).
- 30 Xie, Q. *et al.* Fast water transport in graphene nanofluidic channels. *Nature nanotechnology*
13, 238-245 (2018).
- 31 Li, Y., Alibakhshi, M. A., Zhao, Y. & Duan, C. Exploring ultimate water capillary evaporation in
nanoscale conduits. *Nano Letters* **17**, 4813-4819 (2017).
- 32 Alibakhshi, M. A., Xie, Q., Li, Y. & Duan, C. Accurate measurement of liquid transport through
nanoscale conduits. *Scientific reports* **6**, 24936 (2016).
- 33 Li, Y. *et al.* Ultrafast diameter-dependent water evaporation from nanopores. *ACS nano* **13**,
3363-3372 (2019).
- 34 Jeon, J. *et al.* Layer-controlled CVD growth of large-area two-dimensional MoS₂ films.
Nanoscale **7**, 1688-1695 (2015).
- 35 Tao, L. *et al.* Centimeter-Scale CVD Growth of Highly Crystalline Single-Layer MoS₂ Film with
Spatial Homogeneity and the Visualization of Grain Boundaries. *ACS Appl Mater Interfaces* **9**,
12073-12081, doi:10.1021/acsami.7b00420 (2017).
- 36 Gurarlan, A. *et al.* Surface-energy-assisted perfect transfer of centimeter-scale monolayer
and few-layer MoS₂ films onto arbitrary substrates. *ACS nano* **8**, 11522-11528 (2014).
- 37 Jeon, J. *et al.* Controlling grain size and continuous layer growth in two-dimensional MoS₂
films for nanoelectronic device application. *IEEE Transactions on Nanotechnology* **14**, 238-
242 (2015).
- 38 Yu, H. *et al.* Wafer-Scale Growth and Transfer of Highly-Oriented Monolayer MoS₂
Continuous Films. *ACS Nano* **11**, 12001-12007, doi:10.1021/acsnano.7b03819 (2017).
- 39 Kim, T. *et al.* Wafer-scale production of highly uniform two-dimensional MoS₂ by metal-
organic chemical vapor deposition. *Nanotechnology* **28**, 18LT01, doi:10.1088/1361-
6528/aa6958 (2017).
- 40 Kang, K. *et al.* High-mobility three-atom-thick semiconducting films with wafer-scale
homogeneity. *Nature* **520**, 656-660, doi:10.1038/nature14417 (2015).
- 41 Zhu, D. *et al.* Capture the growth kinetics of CVD growth of two-dimensional MoS₂. *npj 2D*
Materials and Applications **1**, 8 (2017).
- 42 Hu, Z. *et al.* The role of oxygen atoms on the excitons at the edges of monolayer WS₂. *Nano*
letters (2019).
- 43 Cain, J. D., Shi, F., Wu, J. & Dravid, V. P. Growth mechanism of transition metal
dichalcogenide monolayers: the role of self-seeding fullerene nuclei. *ACS nano* **10**, 5440-
5445 (2016).
- 44 Li, Y. *et al.* Site-Specific Positioning and Patterning of MoS₂ Monolayers: The Role of Au
Seeding. *ACS nano* **12**, 8970-8976 (2018).
- 45 Thakur, M. *et al.* Wafer-Scale Fabrication of Nanopore Devices for Single-Molecule DNA
Biosensing using MoS₂. *Small Methods*, 2000072 (2020).
- 46 Casillas, G. *et al.* Elasticity of MoS₂ Sheets by Mechanical Deformation Observed by in Situ
Electron Microscopy. *The Journal of Physical Chemistry C* **119**, 710-715,
doi:10.1021/jp5093459 (2015).
- 47 Rego, K. & Meunier, V. Carbon nanotube knots. *AIP Advances* **9**, 025030,
doi:10.1063/1.5088145 (2019).
- 48 Wang, S. *et al.* Shape evolution of monolayer MoS₂ crystals grown by chemical vapor
deposition. *Chemistry of Materials* **26**, 6371-6379 (2014).

49 Manzeli, S., Allain, A., Ghadimi, A. & Kis, A. Piezoresistivity and strain-induced band gap tuning in atomically thin MoS₂. *Nano letters* **15**, 5330-5335 (2015).

Methods

Wafer-scale fabrication of freestanding SiN membranes with nanopores. The wafers were made by deposition of 50 nm thick medium-stress SiN on 300- μ m-thick and 500- μ m-thick Si (100) wafers that contain a 2- μ m-thick wet thermal SiO₂ grown on them. Deposition of silicon nitride was performed at the Lurie Nanofabrication Facility (LNF). We used e-beam lithography with positive resists (ZEP 520A, ZEON Corporation, Tokyo, Japan) to pattern the entire wafers with circles with diameters in the range of 50-100 nm, 5 mm rectangular pitch. After etching the SiN with RIE, we used photolithography and backside alignment to pattern the other side of wafer to expose windows for potassium hydroxide (KOH) etching. After an RIE step to etch the SiN, we used a single-side etcher to remove the 2- μ m-thick SiO₂ layer using buffered oxide etch (BOE 6:1, J.T. Baker Chemicals, #5569-03) for 40 minutes. Next, the wafers were etched by KOH (30% w/w, Fisher Chemical, #P246-3) at 70°C to obtain the freestanding SiN/SiO₂ membranes. In order to remove the SiO₂ layer under the SiN membranes, the membrane side of the wafer was spin-coated with PMMA (495 PMMA A4, MicroChem) and baked on a hotplate at 160°C for 2 minutes to protect the aperture vicinity against BOE, and then the underlying silicon oxide layer was etched by BOE. The PMMA was later removed by warm acetone immersion (60 minutes, 45°C). Fabrication of wafers with micro-apertures (Supplementary Fig. 14.a) is very similar, the only difference being the use of photolithography to pattern the micro-apertures. After fabrication wafers were cleaned using a hot piranha solution for 15 minutes (H₂SO₄:H₂O₂, 2:1), thoroughly rinsed with deionized water, and baked on a hotplate at 200°C. Wafers were briefly

etched by RIE (Technics Micro-RIE, series 800) for 10 seconds using Ar/SF₆ gas mixture (50 W, 200 mTorr) before growth.

Chemical Vapor Deposition. MoO₂ (Molybdenum(IV) oxide, 99%, Sigma-Aldrich, #234761) and sulfur powders (Alfa Aesar, -100 mesh, 99.5%, #33394) were used in CVD growths after carefully weighing. We used 40 mg MoO₂ in a typical growth. Given the small amount of powder that must be spread over a large area (40 mg MoO₂), we mixed the MoO₂ powder with isopropanol (IPA, Fisher Chemical, #A416-4) and sprayed it over the source wafer which yielded excellent uniformity (Fig. 4d). Fast evaporation of IPA after spray is the key reason behind this choice of solvent. The amount of MoO₂ was verified by weighing the source wafer before and after the spray, following wafer drying. Alternatively, the MoO₂ can be manually spread on the source wafer in a uniformly thin layer. Uniform supply of sulfur is an even more important factor for large scale uniform MoS₂ growth, as sulfur vapor can only diffuse from the wafer edges toward the center (Fig. 4e inset) which creates a radial non-uniformity with higher coverage at the edges and lower coverage and sulfur deficient growth towards the center. We fabricated a perforated wafer containing an array of tapered square through-holes that allowed diffusion of sulfur through the source wafer (Figs. 4d,e) These holes were 1.5 mm wide on the large end of the taper, 0.8 mm wide on its small end, with 5 mm pitch. This technique significantly improved the MoS₂ coverage and flake size uniformity across 4-inch wafers.

Growth was carried out in Argon environment in a 5-inch OD CVD tube (PlanarGROW-5M, PlanarTech, Supplementary Fig. 1), with 750 Torr pressure, and 1000 SCCM flow rate, with a temperature profile shown in Supplementary Fig. 3. The optimal gap between the source and target wafers for high-coverage growth was

found to be 5 mm. A change in the gap size as large as 0.5 mm, and in the amount of MoO₂ as much as 5 mg results in completely distinguishable growths, in terms of MoS₂ flake size and coverage. We also note that increasing the furnace temperature to up to 800°C further improved the coverage (Supplementary Fig. 18) due to increasing sublimation rates of MoO₂. Since both furnaces have to operate at 750°C, we rely on the radiative and convective heat from the furnaces to melt the sulfur. A quartz sulfur boat was placed at a 23 cm distance from the edge of the left furnace (Supplementary Fig. 1). Given the strong temperature gradient in the CVD tube outside the furnace zone, the location of the boat is critical in determining the sulfur kick-in time (Supplementary Fig. 5), which is essential for a good growth. We placed the boat at a height in the tube above the axis where convection becomes the dominant mode of heating. By placing the boat on-axis and closer to the edge of furnace, radiation effects become dominant, which can overheat the sulfur boat.

We note that following a CVD run wafers cannot be reused, since complete removal of the Mo-containing particles from the wafers after the first growth was not possible, which resulted in these particles seeding growth in the next run, which biased the growth evaluation. Moreover, when a growing flake meets these particles, the growth is terminated, and as a result we observed smaller flakes when reusing a wafer even after extensive cleaning (Supplementary Fig. 19). Statistics of flake size and the substrate coverage with flakes were obtained by programming a microscope equipped with a motorized stage. The entire area of each wafer was scanned at a 2.5 mm pitch and at each location an image was captured. These images were fed to an image processing program written in MATLAB which recognized flakes in an unsupervised manner (Supplementary Fig. 20). The results were then assembled to show the growth map on each wafer and quantify the growth.

Computational Fluid Dynamics Analysis. The steady-state laminar Navier-Stokes equations as well as the energy equation were solved in a 3D argon-filled quartz tube with 4.5-inch inner diameter using ANSYS/Fluent package. The pressure-temperature relation follows the ideal gas law and gravity is accounted for. The boundary conditions are constant temperature at the location of furnaces and natural convection over the areas of the tube that are exposed. A constant convection coefficient of $8 \text{ W/m}^2\cdot\text{K}$ was used for calculations. This value was obtained from the empirical relation for horizontal tubes and is valid over the expected range of temperature. The metal caps in the left and right part of the tube are water-cooled and are maintained at $\sim 50^\circ\text{C}$. We used the ANSYS/Fluent finite volume package for solving this problem, and post-processing the data. We note that the obtained temperature values are the maximum tube temperature values that can only be achieved when it reaches the steady-state, but actual growth occurs when the tube is still in a thermally transient state.

Conductance and noise measurements. The MoS_2 chips were mounted in a flow cell which separates the two sides of the membrane, so that ionic current can only be established through the membrane. Two Ag/AgCl electrodes were inserted in the *cis* and *trans* chambers, which were both filled with 400 mM KCl Tris-buffered to pH 8, and a voltage bias was applied to establish an ionic current. The current was recorded using a Chimera VC100 amplifier (Chimera Instruments LLC), digitized at 4.17 M sample/s and digitally low-pass filtered. We used MATLAB to calculate the noise spectra.

Data availability

Data is available from the corresponding authors upon request.

Acknowledgements

Fabrication of wafer-scale apertures was performed in part at the Cornell NanoScale Facility (CNF), a member of the National Nanotechnology Coordinated Infrastructure (NNCI), which is supported by the National Science Foundation (Grant NNCI-2025233). Wafer deposition of silicon nitride was performed at the Lurie Nanofabrication Facility (LNF). We also acknowledge the Kostas Advanced Nano-Characterization Facility (KANCF) at Northeastern University for use of their facilities, and Dr. Wentao Liang for HAADF-STEM imaging. We thank Dr. Ken Healy and Dr. Ping Xie for useful discussions of the methods. We are grateful to Prof. Swastik Kar for use of PL and Raman setup, and Levi S. Gershon for programming the microscope stage.

Author contributions

M.A. and A.V. performed the high coverage MoS₂ growth in a large tube. M.A. and X.K. designed experiments and analyzed the results. D.C. performed the simulations of MoS₂ growth in pores. M.A. performed the growth on aperture, TEM imaging, and the nanopore sensing. Z.Z. contributed to TEM inspection, as well as wetting and stabilizing the flakes in buffer. V.M. performed the simulations. M.A., M.W., and V.M. drafted the manuscript. All authors reviewed and edited the manuscript.

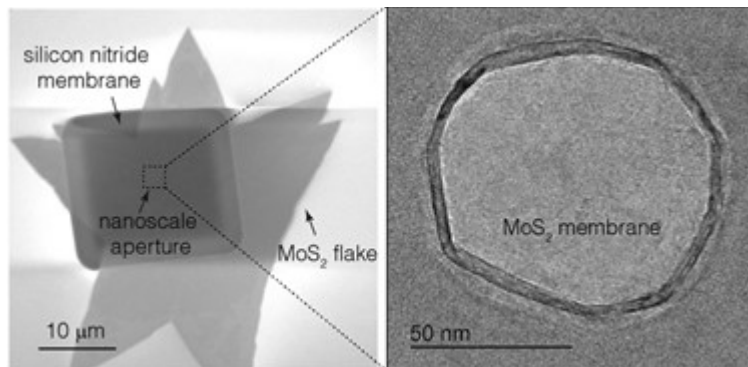
Competing interests

This work was funded by Oxford Nanopore Technologies plc, Oxford, United Kingdom.

Additional information

Supplementary information is available for this paper online.

Correspondence and requests for materials should be addressed to M.A. and M.W.



In this manuscript, the authors propose a method to scale up freestanding synthesis of MoS₂ sheets on 100 mm diameter silicon wafers that have hundreds of nanoapertures. The MoS₂ sheets cover the apertures to form ultrathin membranes that are useful in nanopore sensing.